Austenite-martensite interfacial patterns and energy dissipation of phase transformation in Ni-Mn-Ga single crystal

Chengguan Zhang, Xue Chen, Xingke Gao, François Brisset, Olivier Hubert, Yongjun He

Austenite-Martensite interfacial patterns and energy dissipation of phase transformation in Ni-Mn-Ga single crystal

Chengguan Zhang[1], Xue Chen[2], Xingke Gao[3], François Brisset[3], Olivier Hubert[3], Yongjun He[1,*]

[1] *LMI,UME, ENSTA Paris, Institut Polytechnique de Paris, 91120 Palaiseau, France*

[2] *Faculty of Engineering and Environment, Northumbria University, Newcastle Upon Tyne, UK*

[3] *LMPS, Université Paris-Saclay, CentraleSupélec, ENS Paris-Saclay, CNRS, 91190 Gif-sur-Yvette, France.*

* Corresponding Author. Email address: yongjun.he@ensta-paris.fr (Y.J. He)

Abstract

The martensitic phase transformation occurs in Shape Memory Alloys (SMA) via the nucleation/propagation of the Austenite-Martensite interface (A-M interface), which is a transition region (domain) between the two coexisting phases. For providing compatibility, the transition region consists of various martensitic twin structures (laminates), forming different interfacial patterns, such as parallel laminates and branching laminates. Due to the energy accumulation in the interfacial structures (e.g., elastic mismatch and twin-boundary surface energy), the interfacial patterns should be relevant to the driving force (energy dissipation) and the associated kinetics of the phase transformation. In this paper, we adopt a special thermal loading, small-temperature-gradient "heating-cooling-reheating", to control the A-M interface's forward and reverse propagation to generate different interfacial patterns in a Ni-Mn-Ga single crystal SMA with the observation on the twin structures (by optical microscope and SEM) and the InfraRed measurement on the temperature hysteresis of the interface propagation (for characterizing the thermal driving force). Simple energetic analysis indicates that the thermal driving force (energy dissipation) is directly related to the stored energy in the interfacial structure, particularly the large mismatch elastic energy near the habit plane. This study not only provides the details of the various interfacial patterns and their dependence on the

loading path, but also indicates the driving force and the associated mechanism about the pattern evolution to understand the phase transformation process.

Keywords: austenite-martensite interface, energy dissipation, interfacial structure, martensitic transformation, temperature hysteresis, shape memory alloy.

1. Introduction

Ni-Mn-Ga single crystal is a typical magnetic Shape Memory Alloy (SMA), which has been intensively studied from atomic scale to macroscopic scale [1-10] among many others. Its special properties come from the martensitic phase transformation and the associated martensite twinning structures. Belonging to the 1st order phase transformation, the martensitic phase transformation of Ni-Mn-Ga single crystal occurs via the nucleation/propagation of an interface separating two coexisting phases (austenite and martensite) [11-15]. As shown in Fig. 1(a), while the austenite phase has the cubic symmetry, the martensite phase has approximately tetragonal symmetry with three variants of the short axis along different directions. It has been well recognized that the austenite is generally incompatible with any one of these martensite variants. So, the austenite-martensite interface is not mathematically sharp, but a diffuse interfacial region consisting of a twin as shown by the experimental observation in Fig. 1(b) and 1(c) from the previous study [12]. Here, the twin structure (composition) depends on the single martensite variant, which coexists with the austenite phase during the phase transformation. That is to say, the interfacial structure (twin M_1M_3 in Fig. 1(b)) separating the austenite from the martensite variant M_1 is not the same as that (i.e., twin M_2M_3 in Fig. 1(c)) between the austenite and the martensite variant M_2. As shown in Fig. 2 of the basic result from the compatibility analysis on the martensitic tetragonal symmetry [16, 17], there are only six possible twin structures to form such compatible austenite-martensite interfaces (also called habit planes). That means, the composition (the twins) of the diffuse Austenite-Martensite interface (A-M interface) is not unique; but the various interfacial structures (twin structures) are related to each other by the symmetry of the martensite phase. Due to the symmetry, it is expected that all the six types of A-M interfaces should have the same properties (such as the driving force, energy dissipation, for the interface propagation).

However, our recent study [11, 18] demonstrated that the interfacial structure also depends on the loading path as shown in Fig. 3, where the A-M interface consists of the parallel (branching) twinning laminates in the forward (reverse) martensitic phase transformation driven by cooling (heating). The different patterns (different interfacial structures) imply the different energy stored (accumulated) in the diffuse A-M interface [13, 14, 19-24]. Such interfacial energy is related to the driving force (energy dissipation) for the phase transformation. Then, a question naturally arises: Can the various interfacial patterns lead to significantly different energy dissipation of the phase transformation?

In this paper, we try to answer this question by careful experiments to identify the details of the interfacial structures during heating and cooling with the observation of high-resolution optical camera and SEM. Moreover, InfraRed (IR) camera was utilized to measure the temperature hysteresis for the forward and reverse propagations during the heating-cooling cycle to determine the thermal driving force (dissipation) of the phase transformation. Based on the experimental observation on the interfacial structures, we estimate the energy stored/accumulated in the diffuse interface. Finally, we can understand the interfacial pattern evolution and the associated energy dissipation by comparing the microscopic energy analysis of the interfacial structure with the macroscopic measurement of the temperature hysteresis (energy dissipation).

In the following, Section 2 describes the basic material properties and the experimental procedures. Section 3 reports the experimental results. Section 4 includes the theoretical energy analysis and discussion. Section 5 includes a summary and conclusions.

2. Material and experimental procedures

The specimen applied in the current study is a $Ni_{50}Mn_{28}Ga_{22}$ (at. %) single crystal rectangular bar ($1\times2.5\times20$ mm^3, from Goodfellow, the same batch as [18]) whose faces have been cut approximately along the {100} plane of the parent austenite phase. The specimen's characteristic transformation temperatures M_s,M_f, A_s, and A_f are 35.5℃, 33.7 ℃, 40.1 ℃, and 41.6 ℃, respectively, measured by Differential Scanning Calorimetry (DSC). At low temperatures ($< M_f$), the material is in the martensite phase which can be considered approximately tetragonal symmetry with two long axes (denoted as "*a*") and one short axis (denoted as "*c*") as shown in Fig. 1(a); at high temperatures ($>A_f$) the material

is in the cubic austenite phase whose lattice parameter is denoted as "a_0". The lattice parameters utilized in this study are $a \approx 5.95$ Å, $c \approx 5.61$ Å, and $a_0 \approx 5.84$ Å according to [6, 25, 26]. Before the test, the specimen can be set to M_3 single variant by applying a magnetic field (~0.84 Tesla) along the specimen's z-axis.

To perform the IR measurement and the optical observation on a single propagating interface, we utilized the setup in Fig. 4(a). The specimen's one end is laid on an aluminum plate (connected with a heater) while the other one is laid on a plastic support to avoid constraint; so, the specimen can extend or shrink freely during the phase transformation. The cyclic quasi-static phase transformation can be realized in a specimen's specific area, i.e., the observation area, by controlling the heater's temperature change slowly (with a rate of 0.1 °C/min) between room temperature and 65 °C. A K-type thermal couple is put inside the aluminum plate to monitor the temperature of the specimen's right end as shown in Fig. 4(b), where the thermal loading includes two heating processes and a cooling process.

During the quasi-static thermal loading (slow heating/cooling), the propagating interface with the twinning laminates was captured by a camera (OV48C, OmniVision) via an optical microscope (AX70, Olympus) equipped with polarized light. After capturing the interfacial twinning laminates, we put a candle black layer on the specimen's top x-y plane to increase the specimen's IR emissivity (with a measuring error of ± 0.2 °C) and measured the temperature hysteresis during the heating-cooling cycle by an infrared camera (FLIR X8501SC). Because the resolution of the optical camera is limited to around 0.15 μm, we also utilized SEM (with the resolution of 0.02 μm, Supra 55VP, Zeiss) to observe the fine laminates very close to the habit plane.

3. Experimental results

The results of the interfacial twin microstructure and the temperature hysteresis are reported in the following two subsections, respectively.

3.1 Evolution of interfacial structures

The experiment includes three processes: the 1st heating process, the cooling process, and the 2nd heating process. The optical observations on the diffuse interface evolutions of the three processes

were recorded into three movies (Movies 1, 2 and 3 in the supplementary material). The main features of the interfacial patterns are summarized in Fig. 5.

It is seen from the specimen's States 1 and 2 in Fig. 5(a) that, during the 1st heating process, there is a large interfacial region forming a branching laminate (see the global view (I) and the magnified view (i)); the spacing of the laminae changes from >70 μm to <10 μm. It is interesting to note that, during the propagation of the diffuse interface, the size of the interfacial region (i.e., length of the branching pattern along the x-direction) is nearly unchanged (around 2 mm). That means, the interfacial region translates (propagates) from the right to left keeping the branching pattern during the heating-induced martensite to austenite ($M_3 \rightarrow A$) phase transformation. Before the diffuse interface reaching the specimen's left end, we start the cooling process.

It is seen from States 3 and 4 in Fig. 5(b) that, the cooling-induced austenite to martensite phase transformation leaves a region forming a parallel laminate (see the global view (II) and the magnified view (ii) and (iv)), where the laminae spacing is less than 5 μm. It is also indicated by the global view (III) and the magnified view (iii) that the newly generated parallel pattern can smoothly connect to the residual branching pattern, the remaining branching laminate after the 1st heating process. Similarly, before the interface reaching the specimen's right end, we start the 2nd heating process.

States 5 and 6 in Fig. 5(c) indicate that the heating-induced propagating interface moves back into the residual parallel pattern, the remaining parallel laminate after the cooling process, with the small active zone of a new branching pattern (see the magnified view (v) and Movie 3). Such small active zone translates (propagates) leftward, keeping its size unchanged (around 50 μm along the *x*-direction).

Remark: *Comparing Fig. 5(a) and 5(c), we can see that the active zone of the propagating interface depends on the material states at both sides of the interface. Particularly, when there is large incompatibility (such as the incompatibility between austenite and M_3 in Fig. 5(a)), the active interfacial region can be large (around 2 mm); by contrast, when there exists only slight incompatibility, such as Fig. 5(c) where austenite is nearly compatible with the parallel laminates, the active interfacial region is small (around 100 μm).*

In comparison with the compatibility results of the habit planes in Fig. 2, the above optically observed orientations of the interface (habit plane) and the twin boundaries (the traces of the laminates) imply that the laminates in Fig. 5 consist of the two martensite variants M_3 and M_2 with a volume ratio of around 68%: 32% (about 2:1). More details about the determination of the martensite states by the compatibility analysis and other methods such as DIC (Digital Image Correlation) can be found in previous papers [12, 16].

To quantitatively characterize the interfacial structures, especially distinguish the parallel and the branching patterns, we define some parameters in Fig. 6(a). In each sampling box, a representative area with the width Δy (around 0.5 mm) at different distances (x) from the interface (habit plane), the number of laminae can be counted and denoted as n; then the laminae density (ρ) can be calculated by $\rho = \frac{n}{\Delta y}$ (or the laminate period $\lambda = \frac{\Delta y}{n}$). Moreover, the percentage (η) of M_2 laminae in the representative area can be estimated by ImageJ software; then, the width of a M_2 lamina can be determined by $d = \eta\lambda = \frac{\eta}{\rho}$. With these parameters, the interfacial patterns of the above States 1~5 can be described by Figs. 6(b) ~ 6(e).

Fig. 6(b) shows the profiles of the M_2 percentage (η), the laminae spacing period (λ), the M_2 lamina's width (d), and the laminae density (ρ) for State 1 (also State 2) during the 1st heating process. It is seen from the percentage profile that, when x increases from zero, η decreases drastically from the value around 0.3 (the required volume fraction to be compatible with the austenite). All the parameters (η, λ, d, and ρ) become zero only when x > 2 mm. That means, the size of the active branching pattern in the 1st heating is as large as 2 mm. On the other hand, the global features of State 5 in the 2nd heating in Fig. 6(c) seem to be significantly different from those in Fig. 6(b). But, if zooming into the range close to the habit plane (x < 0.5 mm) to compare States 1 and 5 as shown in Fig. 7(a), we can see that, within the narrow range around 100 μm (about the small active zone of the 2nd heating), all the features (the parameters η, λ, d, and ρ) have the same values for both States 1 and 5. In other words, there is a characteristic zone of the heating-induced phase transformation, whose features (the parameters η, λ, d, and ρ) of the interfacial structure are independent of the initial/boundary condition such as the initial state M_3 or the residual parallel laminate.

Similarly, the global features of States 3 in Fig. 6(d) are obviously different from those of State 4 in Fig. 6(e). But their magnification of the range $x < 0.5$ mm in Fig. 7(b) indicates that all the features of the two states have almost the same values when $x < 100$ μm. In other words, during the cooling-induced propagation, changing from State 3 to State 4, the interfacial structure close to the habit plane keeps unchanged, implying the same driving force for both States 3 and 4.

Due to the resolution limitation, the optical camera cannot clearly distinguish the M_2 laminae of the size $d < 0.5$ μm in Fig. 7. So, we took SEM observation on the laminates close to the habit plane (distance $x < 20$ μm) as shown in Fig. 8(a). It is seen that, while the heating laminate keeps branching up to the fuzzy zone, the cooling laminate cannot keep parallel pattern any more, but becomes also branching. From the parameters of the two patterns (heating and cooling) in Fig. 8(b), we can see that, at the zone very close to the habit plane ($x < 10$ μm), both heating and cooling have very fine laminates: M_2 lamina width d can be smaller than 0.2 μm.

With the above quantification on the interfacial structures, we can follow the spirits of [13, 14] to estimate the energy stored in the interfacial zone and relate the energy to the driving force (energy dissipation) for the interface propagation during the phase transformation [19, 20]. The theoretical discussion will be given in Section 4. To provide experimental data to validate/verify the theoretical discussion/prediction, the following subsection reports the IR measurement on the temperature hysteresis of the phase transformation, which can indicate the energy dissipation of the forward and reverse interface propagation.

3.2 Temperature hysteresis of forward and reverse interface propagation

With the IR camera, the detailed temperature evolutions of the quasi-static propagating interface during the 1st heating, the cooling, and the 2nd heating processes are recorded, respectively, into Movies 4 ~ 6 (supplementary materials) whose typical frames and the associated interface positions are shown in Figs. 9(a) and 9(b). It is noted that, from the interface stick-slip motion in Fig. 9(b), we can identify the temperature for the start of the interface slip motion (denoted as $T^{slip\text{-}start}$) based on the IR images

of Fig. 9(a) for the forward and reverse interface slip motions at the time instants t_i and the interface positions x_i. The data of the IR images of Fig. 9(a) are two-dimensional temperature distributions changing with time ($t_1 \sim t_{19}$). To facilitate observations and comments, we plot the temperature profiles at the center line along the specimen's length direction (x-direction in Fig. 9(a)) for the time instants $t_1 \sim t_{19}$ in Fig. 10. It is found that the slip-start temperature of the heating-induced forward interface propagation ($t_1 \sim t_7$ and $t_{14} \sim t_{19}$) is $T^{\text{slip-start}}_{\text{heating}} = 37.7 \pm 0.2$ °C while that of the cooling-induced reverse interface propagation ($t_8 \sim t_{13}$) is $T^{\text{slip-start}}_{\text{cooling}} = 34.6 \pm 0.2$ °C; their difference (around 3.1 °C) can be considered as the thermal hysteresis of the forward and reverse phase transformation. In Fig. 10(a), it is worth to note that the driving temperature of the 1st heating ($t_1 \sim t_7$) is almost the same as that of the 2nd heating ($t_{14} \sim t_{19}$), around 37.7 °C.

According to the DSC result of the material, the latent heat and the entropy change of the phase transformation can be measured. Particularly, the entropy difference is $\Delta S \approx 1.2 \times 10^5$ J/(m^{3}K) [18, 27]. Considering the above temperature hysteresis $\Delta T \approx 3.1$ K, the energy dissipation of the heating-cooling cycle is

$$D_{\text{heating-cooling}} = \Delta T \cdot \Delta S \approx 3.1\text{K} \times 1.2 \times 10^5\ \text{J/(m}^3 \cdot \text{K)} \approx 0.37\ \text{MPa}\ or\ 10^6\ \text{J/m}^3 \quad (1)$$

It is interesting to know that this energy dissipation has the same order of magnitude as the energy dissipation of the stress-induced phase transformation in a loading-unloading cycle ($D_{\text{stress}} \approx 0.5$ MPa in [28] and [29]). On the other hand, if we utilize a magnetic field (H) to drive the phase transformation to overcome such energy dissipation, the required magnetic field is:

$$\mu H \cdot \Delta M > D_{\text{heating-cooling}} \quad (2a)$$

$$\mu H > \frac{D_{\text{heating-cooling}}}{\Delta M} = 0.37\ \text{MPa}/0.5 \times 10^5\ \text{A/m} \approx 7.4\ \text{T} \quad (2b)$$

where ΔM ($\approx 0.5 \times 10^5$ A/m) denotes the difference in saturation magnetization between the austenite and martensite phases [30]. Equation (2) means that a large magnetic field (> 7 T) is needed to drive the dissipative phase transformation [31]. It should be noted that, in literature, there are no systematic

reports about the details of the interfacial structure during the stress- or field-induced phase transformation, which might not be the same as that of the thermal loading reported here.

4. Discussion

Based on the observations and the characterizations on the pattern evolution of the interfacial structure in the heating-cooling cycle, our understanding can be summarized into Fig. 11, where the A-M interfacial structure can be divided into three zones: a small fuzzy zone (blurry region) neighboring with the habit plane, a middle zone (0.3 μm ≈ $x_0 < x < x_{end}$ ≈ 100 μm), and a large remote zone (x > 100 μm). Their main features and the associated energy analysis are given in the following subsections.

4.1 Fuzzy zone (x < 0.3 μm)

As shown by the SEM images in Fig. 8(a), there is a blurry region (fuzzy zone) very close to the habit plane. It is expected/conjectured by several research groups [13, 14, 20] that there is large mismatch elastic energy stored in the zone as schematically shown in Fig. 11 (a). It is difficult to calculate accurately the stored energy there. But, with some approximation, the elastic energy density of this zone can be estimated, such as the following Eq. (3) given by [14]:

$$\boldsymbol{U}_{elas}^{fuzzy} = -\frac{1}{4} E\, \varepsilon_{22}^{*M3} \varepsilon_{22}^{*M2} \tag{3}$$

where E is the Young's modulus of both austenite and martensite phases (assuming the same modulus for both phases for simplifying the following calculations); ε_{22}^{*M2} and ε_{22}^{*M3} are the elastic mismatch strains of M_2 and M_3 with the austenite (see Eqs. (A.12) and (A.13) in Appendix). The detailed derivation of Eq. (3) and the associated physical meaning can be found in Appendix A.

While the strains ε_{22}^{*M2} and ε_{22}^{*M3} can be determined quite accurately based on the material lattice parameters (ε_{22}^{*M2} ≈ -0.02 and ε_{22}^{*M3} ≈ 0.0091 from Eqs. (A.12) and (A.13) in Appendix A), the material's Young's modulus is not easy to be determined accurately due to the material softening during the phase transformation [32-34]. In literature, the reported value of the Young's modulus (E) varies a lot [35-37]; usually, the modulus is expected to be within the range:

$$1\ \text{GPa} < E < 10\ \text{GPa} \tag{4}$$

Substituting all these values into Eq. (3), the elastic energy density in the blurry (fuzzy) zone can be estimated as

$$0.05\ \text{MPa} < \boldsymbol{U}_{elas}^{fuzzy} < 0.5\ \text{MPa} \tag{5}$$

Out of the fuzzy zone (e.g., in the middle zone where $x > 0.3$ μm), the elastic mismatch energy would decrease.

4.2 Middle zone ($x_0 < x < x_{end}$)

As shown in Figs. 8 and 11(b), both the cooling and heating patterns have a middle zone consisting of a branching twin laminate. Although branching twins have been widely studied in literature [13, 38-40], there is no simple expression to describe the branching pattern—the profile $\lambda(x)$ in Fig 8(b). Here, with the energy analysis following the spirit of [13], we derive a concise formula to describe the pattern profile $\lambda(x)$ for both cooling and heating cases (Section 4.2.1), and the associated energy analysis (Section 4.2.2).

4.2.1 Pattern profiles

According to [13], the energy density U (energy per unit volume) of the laminate includes two parts: (1) U_{TB}, the surface energy of twin boundaries; (2) U_{elas}, the elastic energy due to the inclination (bending) of the laminae, which depends on the gradient of the laminae spacing (period λ).

$$U = U_{elas} + U_{TB} = a_1\left(\frac{d\lambda}{dx}\right)^2 + \frac{2}{\lambda}\frac{\gamma_{TB}}{cos\,45^\circ} = a_1(\lambda')^2 + \frac{2}{\lambda}\gamma_s \tag{6}$$

where the gradient of the laminae spacing is denoted as $\lambda' \equiv \frac{d\lambda}{dx}$; the effective elastic stiffness a_1, having the dimension as Young's modulus (Pa or J/m³), collects the effects of the elastic constants, the geometry of twins and habit plane, etc.; γ_{TB} is the surface energy of the twin boundary per unit area; $\frac{2}{\lambda\,cos\,45^\circ}$ represents the surface area of the twin boundaries in a unit volume; $\gamma_s \equiv \frac{\gamma_{TB}}{cos\,45^\circ}$, where the

angle 45° is due to twin boundary normal **n**=$[0,\frac{1}{\sqrt{2}},\pm\frac{1}{\sqrt{2}}]$ as shown in Fig. 2(f); the corresponding three-dimensional configuration is shown in Fig. A2(a) of Appendix A; more details about Eq.(6) can be found in Appendix B.

We can obtain the governing equation of the profile $\lambda(x)$ by minimizing the total energy of the middle zone:

$$\text{Min } \int_{x_0}^{x_{end}} U\,dx$$

$$\Rightarrow \quad -a_1(\lambda')^2+\frac{2}{\lambda}\gamma_s = A \tag{7a}$$

$$\Rightarrow \quad -U_{elas}+U_{TB} = A \tag{7b}$$

where the Euler-Lagrange equation has been used and A is a constant to be determined by boundary condition. As shown in Fig. 12, we have the boundary condition at $x = x_{\text{end}}$: $\lambda_{end} \equiv \lambda|_{x=x_{end}}$ and $\lambda'_{end} \equiv \lambda'|_{x=x_{end}} = 0$. So, at this boundary,

$$U_{elas}|_{x=x_{end}} = a_1 \cdot (\lambda'_{end})^2 = 0 \tag{8}$$

The combination of Eqs. (6), (7), and (8) leads to:

$$U|_{x=x_{end}} = U_{TB}|_{x=x_{end}} = A = \frac{2}{\lambda_{end}}\gamma_s \tag{9}$$

With the given constant A in Eq. (9), the profile of laminae spacing λ can be determined by Eq. (7a):

$$\frac{d\lambda}{dx} = \sqrt{\frac{2\gamma_s}{a_1}\left(\frac{1}{\lambda}-\frac{1}{\lambda_{end}}\right)} \tag{10}$$

Solving Eq. (10), we have

$$x = \lambda_{end}\sqrt{\frac{\lambda_{end}\,a_2}{2\gamma_{TB}}}\left(\arcsin\left(\sqrt{\frac{\lambda}{\lambda_{end}}}\right)-\sqrt{\frac{\lambda}{\lambda_{end}}-\left(\frac{\lambda}{\lambda_{end}}\right)^2}\right) \tag{11}$$

where the relations $\gamma_s = \frac{\gamma_{TB}}{cos\,45°}$ and $a_2 \equiv a_1 \cos 45°$ have been used. Detailed derivation and solution procedures of Eqs. (7)-(11) can be found in Appendix B.

It is interesting to note that there is a characteristic length scale in Eq. (11):

$$l = \lambda_{end} \sqrt{\frac{\lambda_{end}\, a_2}{2\gamma_{TB}}} = {\lambda_{end}}^{\frac{3}{2}} (2\gamma_{TB})^{-\frac{1}{2}} {a_2}^{\frac{1}{2}} \equiv {\lambda_{end}}^{\frac{3}{2}} \cdot b \tag{12}$$

where $b \equiv (2\gamma_{TB})^{-\frac{1}{2}} {a_2}^{\frac{1}{2}}$. Utilizing this characteristic length l to rescale the coordinate *x*, we can normalize Eq. (11) as

$$\bar{x} = \arcsin\left(\sqrt{\bar{\lambda}}\right) - \sqrt{\bar{\lambda} - \left(\bar{\lambda}\right)^2} \tag{13}$$

where $\bar{x} \equiv \frac{x}{l}$ and $\bar{\lambda} \equiv \frac{\lambda}{\lambda_{end}}$. While profile $\lambda(x)$ and the associated λ_{end} have been measured in the current experiment (Figs. 8 and 11(b)), the parameter *b* (or the characteristic length l) in Eq. (12) is unknown and needs to be determined by comparing Eq. (13) with the experimental profile $\lambda(x)$ as shown in Fig. 13.

It is surprising in Fig. 13 that, when $l \approx 68\ \mu m$ (or $b = \frac{68\ \mu m}{{\lambda_{end}}^{\frac{3}{2}}}$), the normalized equation, Eq. (13), can describe the branching middle zone not only for the cooling-induced pattern, but also for the heating-induced pattern. The reason should be that the branching twin laminates in the middle zones of both cooling and heating patterns are the result of the competition (trade-off) between the elastic energy and the twin boundary surface energy. But the experiment in Fig. 8(b) also clearly shows the difference between these two patterns: $\lambda_{end}^{heating} = 4.4\ \mu m > \lambda_{end}^{cooling} = 1.6\ \mu m$. As the two patterns share the same characteristic length $l \approx 68\ \mu m$ and the relation $b = \frac{l}{{\lambda_{end}}^{\frac{3}{2}}}$, we can deduce that $b^{heating} < b^{cooling}$, i.e., the effective elastic stiffness $a_2^{heating} < a_2^{cooling}$ (noting $b \equiv (2\gamma_{TB})^{-\frac{1}{2}} {a_2}^{\frac{1}{2}}$ and assuming the same twin boundary energy density γ_{TB} for both heating and cooling). This is reasonable when considering the different material softening behaviours during the heating and cooling-induced phase transformations. During the heating-induced martensite→austenite transformation, the martensite becomes soft (so-called pre-transformation), i.e. the martensite's

effective elastic stiffness $a_2^{heating}$ already becomes small before the martensite twin touching the habit plane, such as in the middle zone. By contrast, during the cooling-induced austenite → martensite transformation, the martensite is the stable phase whose stiffness $a_2^{cooling}$ would be large. In summary, although both the cooling and heating branching twin laminates in the middle zones are governed by the same physical mechanism (competition between the elastic energy and the twin surface energy), the phase-transformation softening and hysteresis make the two patterns apparently different.

4.2.2 Energy dissipation

With Eqs. (6) and (10), we can obtain the expression of the elastic energy:

$$U_{elas} = a_1 \left(\frac{d\lambda}{dx}\right)^2 = 2\gamma_s \left(\frac{1}{\lambda} - \frac{1}{\lambda_{end}}\right) \tag{14}$$

Combining Eq. (14) and the profile $\lambda(x)$ in Fig. 13, we know that, when x decreases (i.e., becoming more close to the habit plane), λ decreases (with finer laminae) and the elastic energy $U_{elas}(x)$ increases until $U_{elastic}^{Fuzzy}$ as schematically shown in Fig. 14. From this elastic energy curve, the interfacial pattern evolution can be understood better. From the material point of view, when the interface (habit plane) passes through the specimen, each material point of the specimen experiences an energy rising-dropping process as shown in the loading path (dashed line) in Fig. 14. During the cooling, the material point (initially in austenite phase) stores a large elastic energy in the fuzzy zone and generates very fine laminae; when the habit plane goes away (i.e., x increases), the fine laminae grow (coarsening by merging the neigbouring twin boundaries) and the stored energy is released/dissipated via the intermittent unstable events — the annihilation/merging of twin boundaries. By contrast, during the heating, the martensite twin splits into fine laminae when coming close to the habit plane (i.e., x decreases); the maximum stored energy is reached in the fuzzy zone and the energy is suddenly released/dissipated when crossing the habit plane.

These unstable processes (nucleation/merging/annihilation of the twin boundaries) lead to the macroscopic energy dissipation such as the temperature hysteresis (e.g., in Fig. 10 of the current experiment) and the stress hysteresis of the stress-induced phase transformation. According to the

suggestion of [19], the energy dissipation $D_{interface}$ of the diffuse interface propagation can be approximately equal to the maximum energy density U_{max} in the interfacial structure, which can be estimated by Eqs. (6) and (7b).

$$D_{interface} = U_{max} = (U_{elas})_{max} + (U_{TB})_{max} = (U_{elas})_{max} + (\mathrm{A} + U_{elas})_{max} = 2(U_{elas})_{max} + \mathrm{A}$$

$$= 2\,U_{elastic}^{Fuzzy} + \mathrm{A} \tag{15}$$

Considering Eqs. (5) and (9), and the material constant $\gamma_{TB} = 6 \times 10^{-3}$ J/m^2 from [14], we find $A \ll U_{elastic}^{Fuzzy}$. So, Eq. (15) can be simply expressed as:

$$D_{interface} \approx 2\,U_{elastic}^{Fuzzy} \tag{16}$$

Then, the total energy dissipation of the forward and reverse interface propagations during a heating-cooling cycle can be approximately estimated:

$$\mathrm{D_{Forward-reverse}} \approx 2\mathrm{D_{interface}} \approx 4\,U_{elastic}^{Fuzzy} \tag{17}$$

Considering Eq. (5), the theoretically estimated energy dissipation of the phase transformation cycle (including forward and reverse interface propagations) is:

$$0.2\ \mathrm{MPa} < \mathrm{D_{Forward-reverse}} < 2\ \mathrm{MPa} \tag{18}$$

It is seen in the measurement of the temperature hysteresis in Section 3.2 that the measured energy dissipation, 0.37 MPa in Eq. (1), is within the theoretically estimated range in Eq. (18).

4.3 Remote zone ($x > x_{end}$)

As shown in Figs. 6(d), 6(e), and 7(b), the cooling-induced interfacial pattern in the remote zone (x > 100 μm) is quite trivial: parallel laminate with only small variation in the period $\lambda^{\mathrm{Cooling}}$, changing very slowly from 1.4 μm (x = 100 μm) to 3 μm (x = 2.5mm). By contrast, the remote zone of the heating case (x > 100 μm) has much more complicated structures because the structures need to be gradually transformed into the single martensite variant (in the 1st heating process in Fig. 6(b)) or into the residual parallel laminate (in the 2nd heating process in Fig. 6(c)). Therefore, the parameters of the

two patterns in Fig. 7(a) show that the two heating processes have significant difference at $x > 100$ μm while they have little difference at $x < 100$ μm. More interesting is that the IR measurement in Fig. 10 shows the same temperature (37.7°C) of the interface propagation in both heating processes. That means, the driving force of the phase transformation doesn't depend on the remote zone of the interfacial structure. In other words, the phase transformation process and the associated austenite-martensite compatibility most affect the middle zone rather than the remote zone.

5 Summary and conclusions

Generally, the phase transformation and the associated martensite-laminate microstructure evolution can be driven by controlling the temperature or/and mechanical stress. Moreover, even without the phase transformation, the external mechanical stress can trigger the martensite reorientation (the material's state changing from one martensite variant to another). Therefore, the thermo-mechanical coupling effect on the austenite-martensite interfacial patterns is a challenging topic and needs more systematic study in the future. To achieve clear understanding on the simplest interfacial patterns in current study, we develop the experiment with only thermal loading (heating/cooling), letting the specimen in the stress-free condition (without external mechanical loading in Fig. 4(a)). The thermal cycle with "heating-cooling-reheating" of a small temperature gradient (less than 1°C/mm) was applied to control the austenite-martensite interface's forward and reverse propagation to generate different interfacial patterns in a Ni-Mn-Ga single crystal SMA. Combining the observed patterns (by optical microscope and SEM), the measured temperature hysteresis (by IR camera), and the simple energetic analysis, we can draw the following conclusions about the interface propagation and the associated driving force (energy dissipation).

- The loading mode (heating/cooling), boundary condition and initial state can influence the formation of the interfacial pattern, especially the "remote" zone that has only weak constraint from the habit plane. The interfacial structure in the "remote" zone can be branching, parallel or their mixtures.

- Due to the strong constraint of the habit plane (the austenite-martensite compatibility), both heating- and cooling-induced interfacial patterns have the same feature near the habit plane: a branching "middle" zone of a size around 100 μm and a small "fuzzy" zone. Particularly, both the heating- and cooling-induced branching laminates of the "middle" zone can be described by a single normalized equation (Eq. (13)), as they are governed by the same physical mechanism—competition between the mismatch elastic energy and the twin laminate surface energy.
- The energy stored in the diffuse austenite-martensite interface (particularly, the maximum energy density U_{max} in the interfacial pattern) is related to the required driving force (energy dissipation) of the interface propagation for the phase transformation, $D_{interface} = U_{max}$ (as in Eq. (15)) and the total dissipation of a heating-cooling cycle (forward-reverse phase transformation cycle) is around two times of the interface-propagation dissipation, $D_{Forward-reverse} \approx 2D_{interface}$ (as in Eq. (17)). Particularly for the current material under study (Ni-Mn-Ga single crystal), $D_{Forward-reverse}$ has the order of magnitude around 0.5 MPa (see Eq. (18)). In other words, only the middle zone and the fuzzy zone (storing large energy) strongly reflect the driving force (energy dissipation) of the phase transformation.

Acknowledgements

Chengguan Zhang would like to acknowledge China Scholarship Council (CSC) for the financial support (NO. 202006890005)

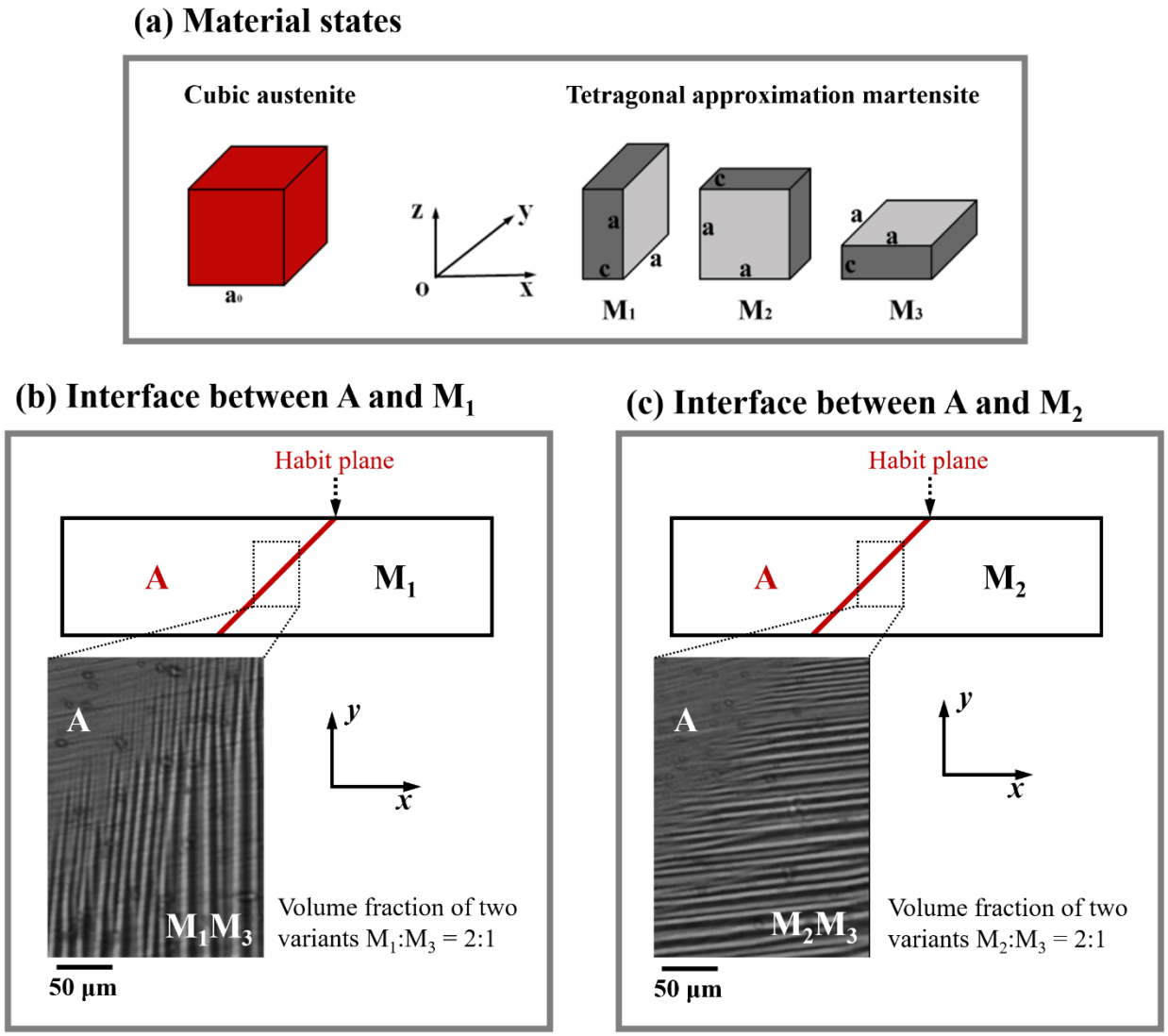

Fig. 1 Material states and the optical observation of the typical interfacial structures — twin laminates (images from [12]).

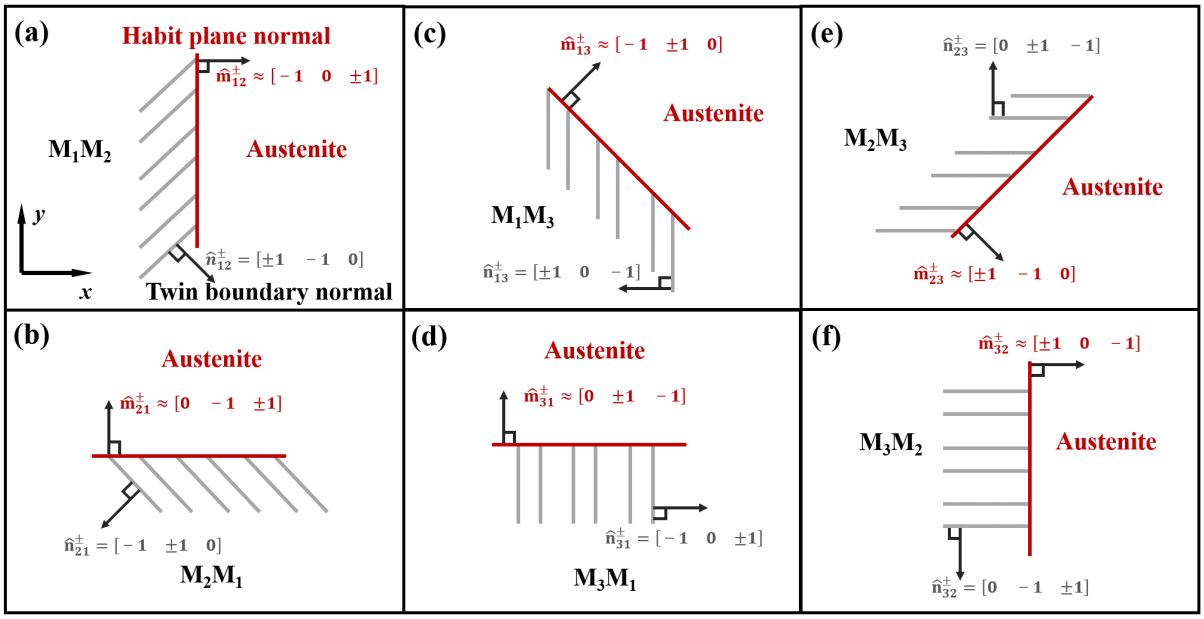

Fig. 2 The traces (projections) of the theoretically predicted habit planes and their associated twin boundaries of the six possible twins on the specimen's *x*-*y* surface from [16].

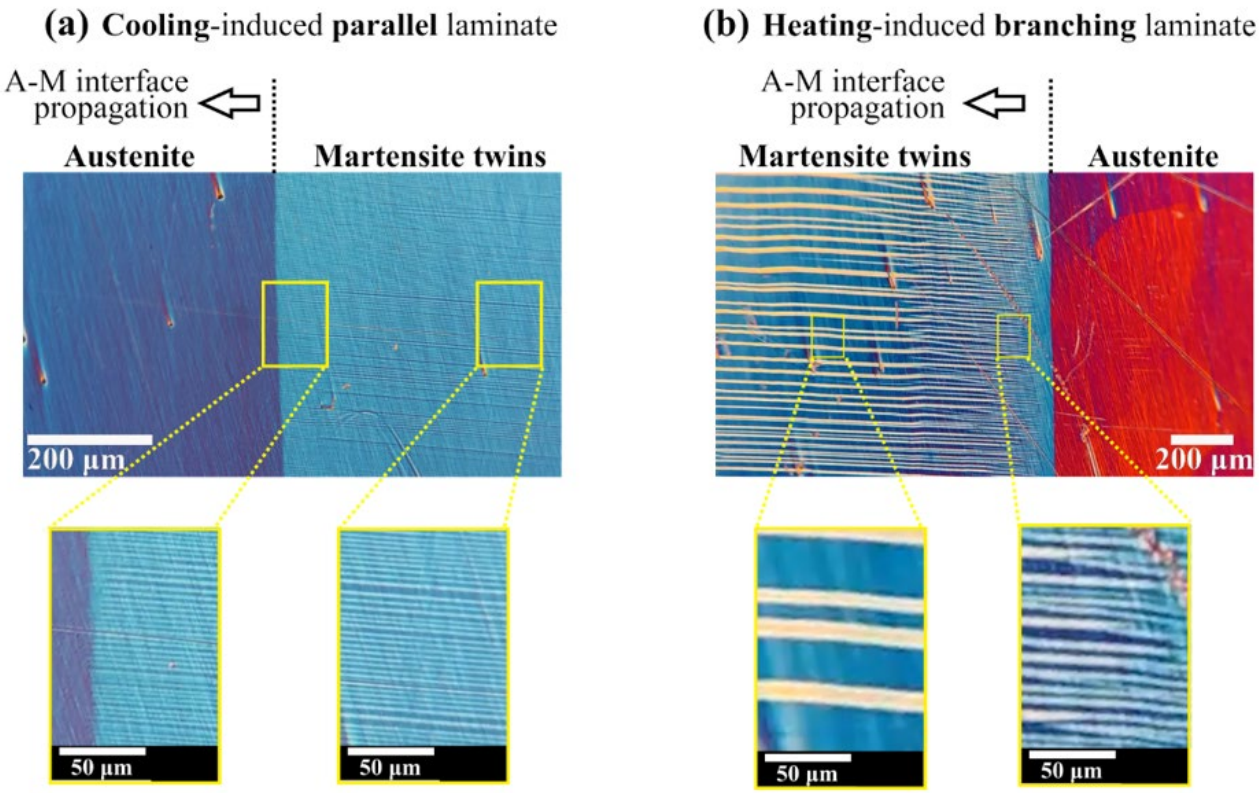

Fig. 3 The dependance of the austenite-martensite interface on loading path from [11].

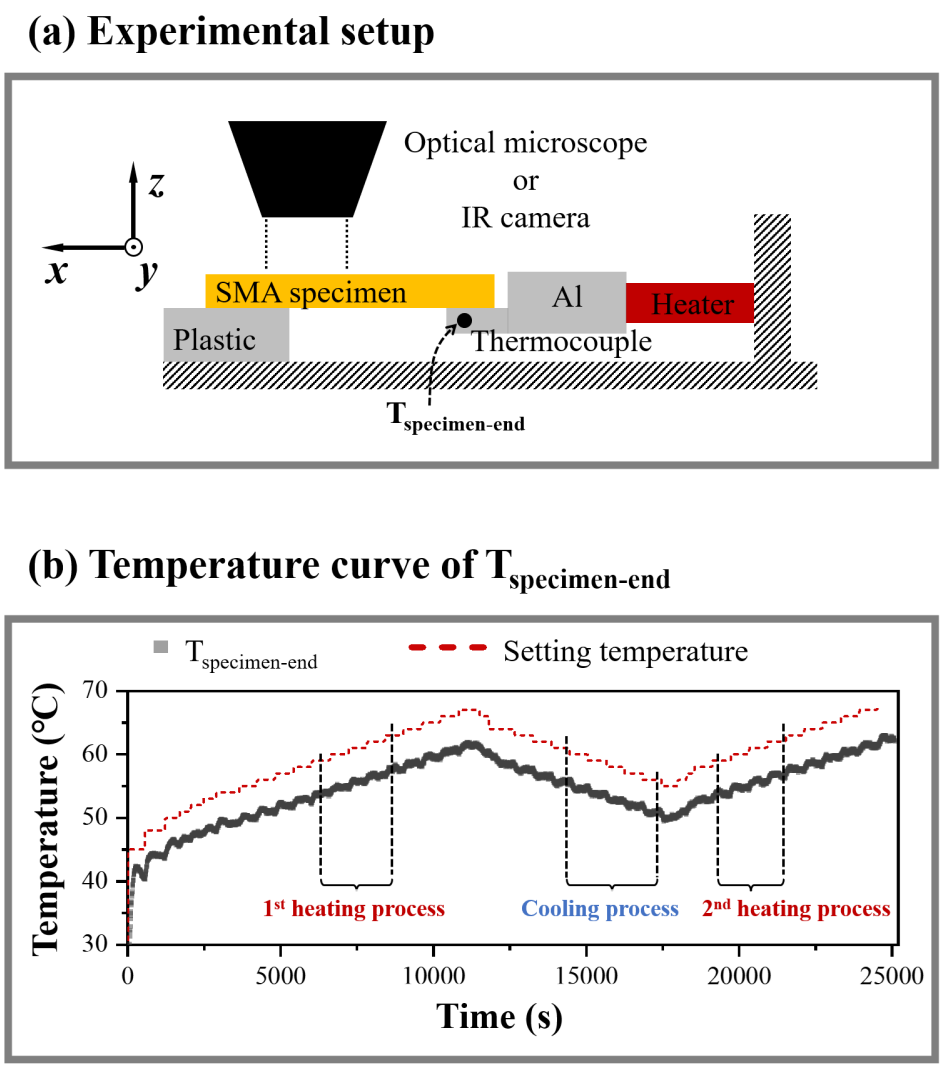

Fig. 4 Experimental setup (a) and the temperature curve of the thermal loading (b).

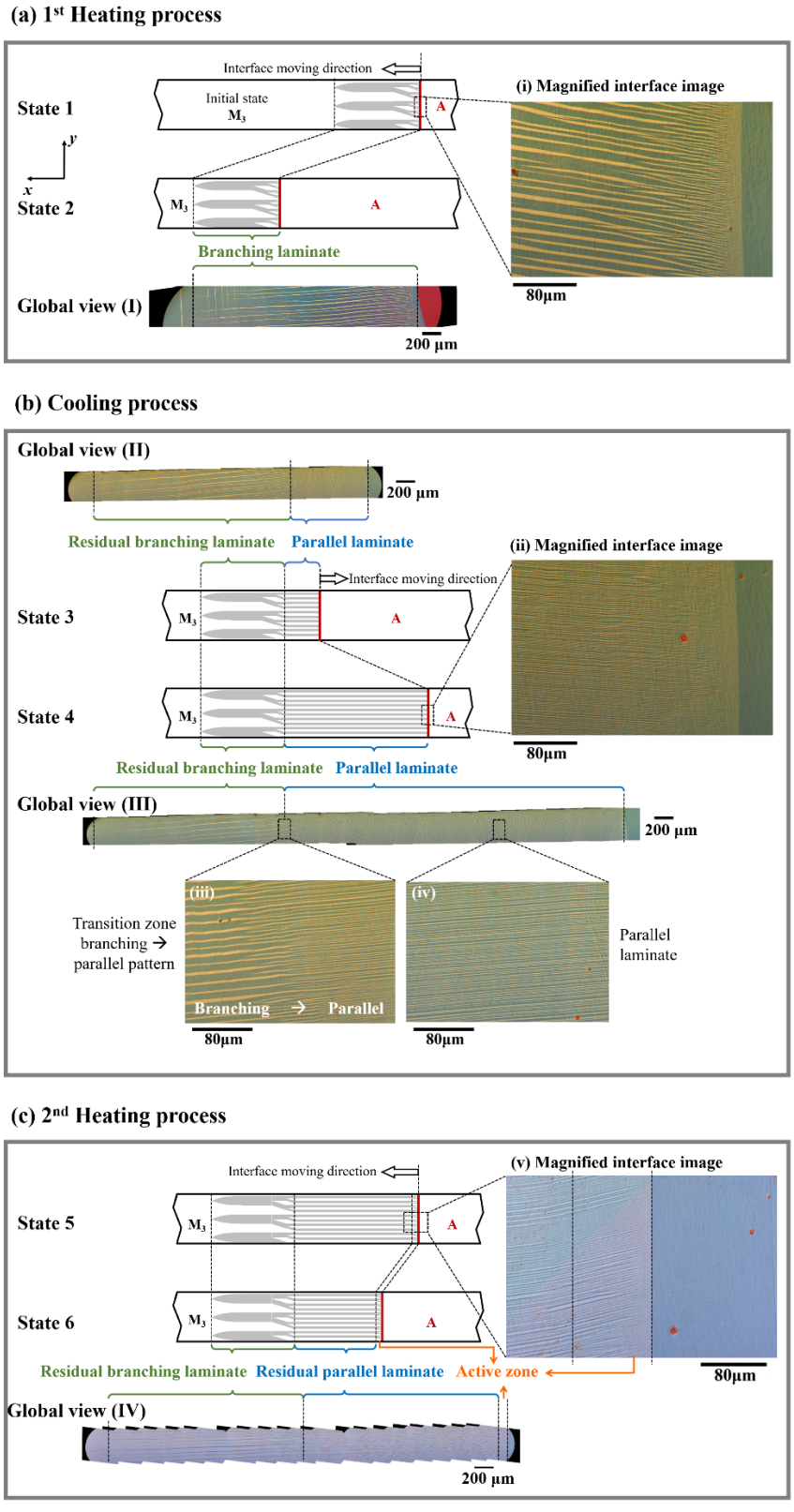

Fig. 5 Global and local views of different interfacial patterns in the experiment including two heating processes and one cooling process.

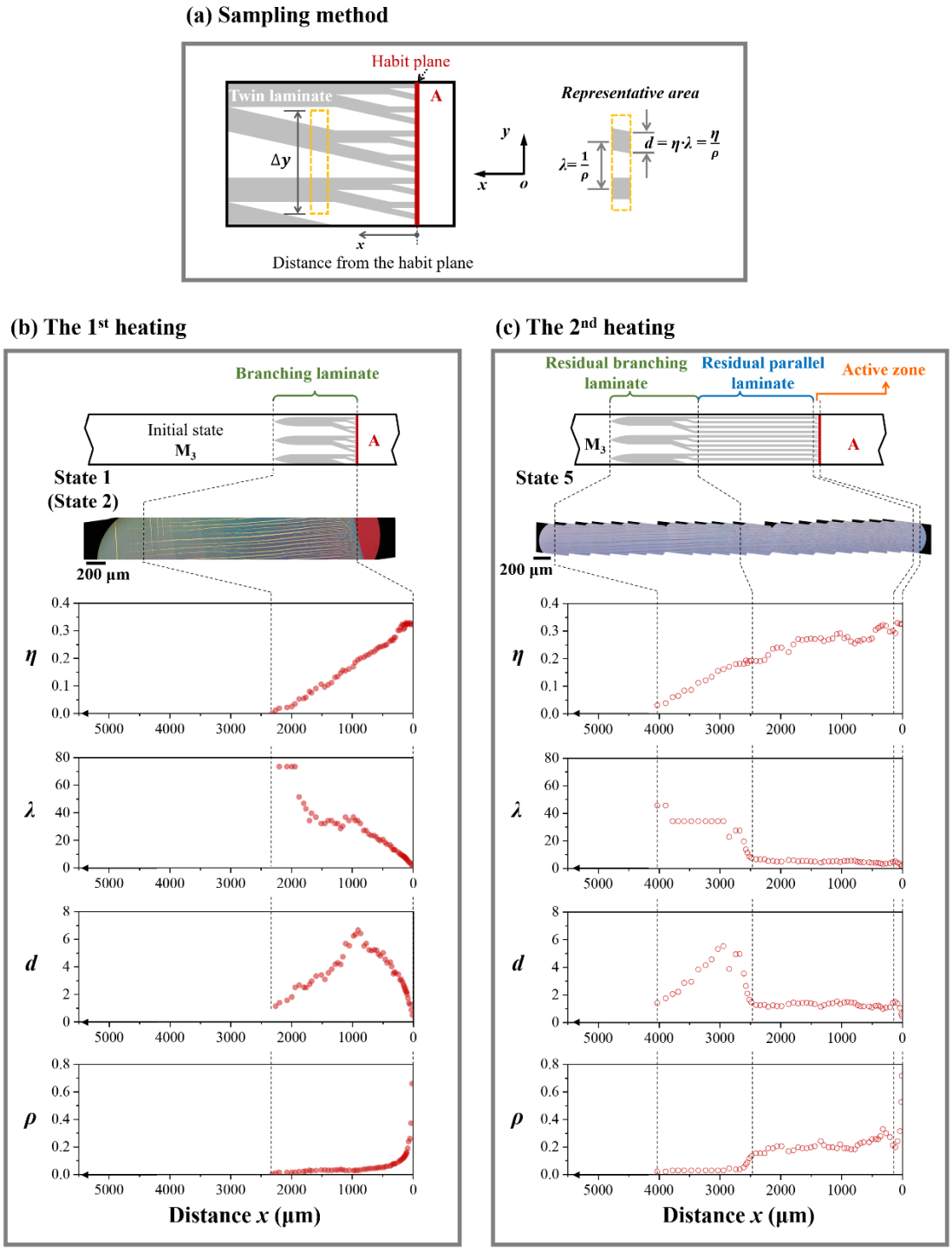

Fig. 6 Quantitative characterization of the interfacial patterns with the parameters: volume fraction of M_2 laminae η, laminae spacing peirod λ (μm), M_2 lamina width *d* (μm), and laminae density ρ (number/μm).

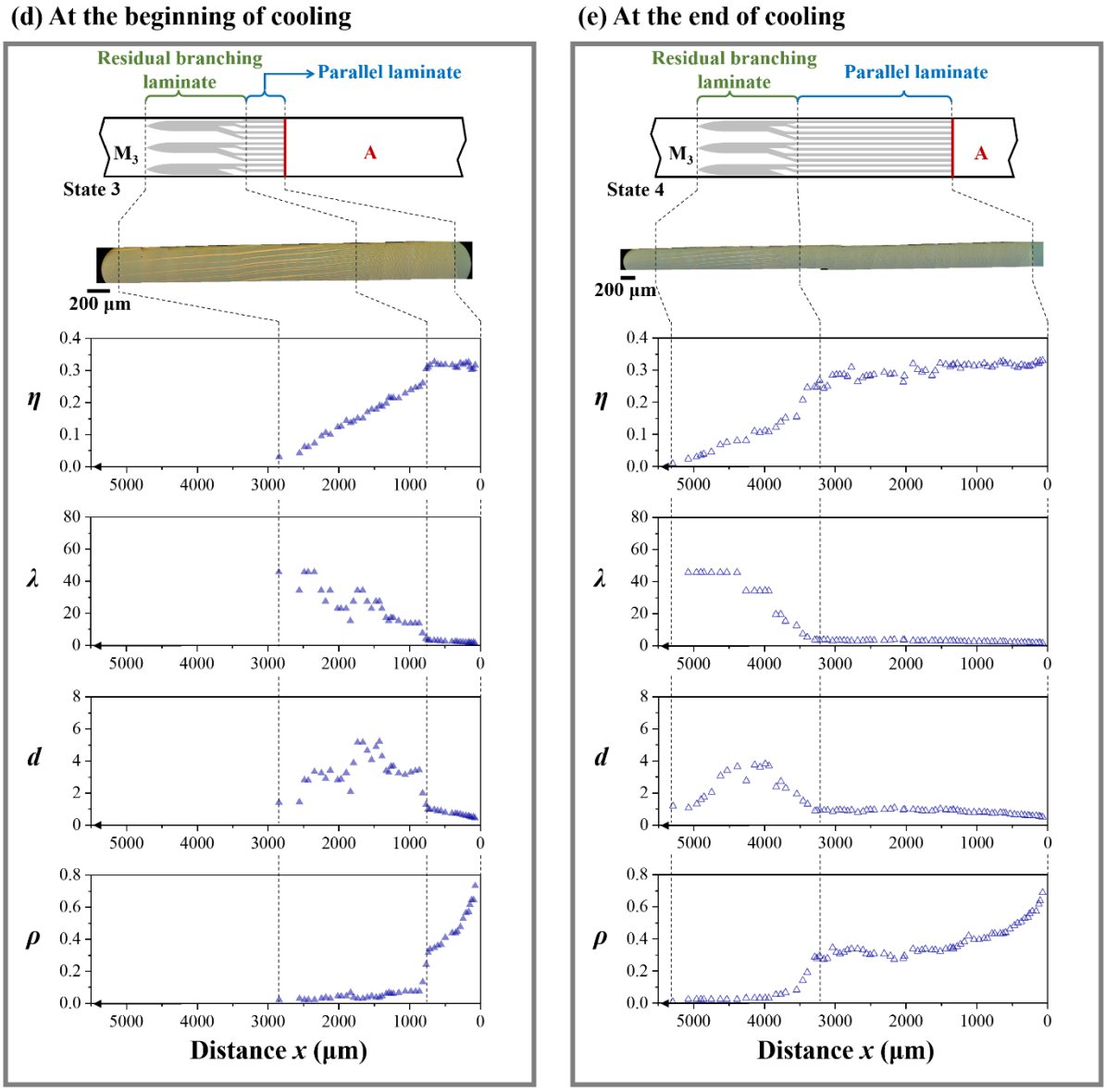

Fig. 6 (continue)

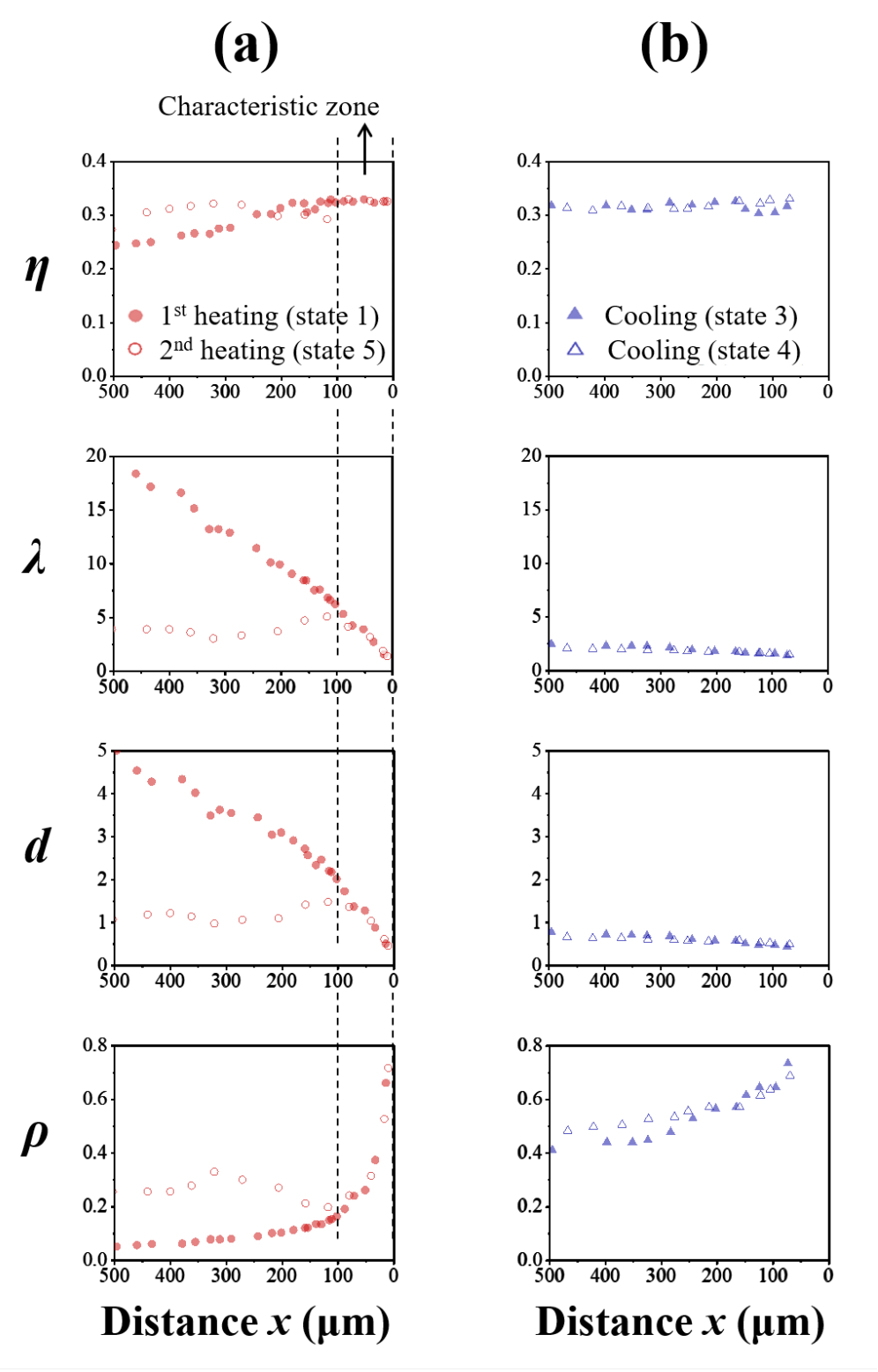

Fig. 7 Magnified views on the distributions of the patterns' parameters at the range close to the habit plane (x < 500 μm). The parameters η, λ, d, and ρ here represent the volume fraction of M_2 laminae, laminae spacing, M_2 laminae width, and laminae density, respectively.

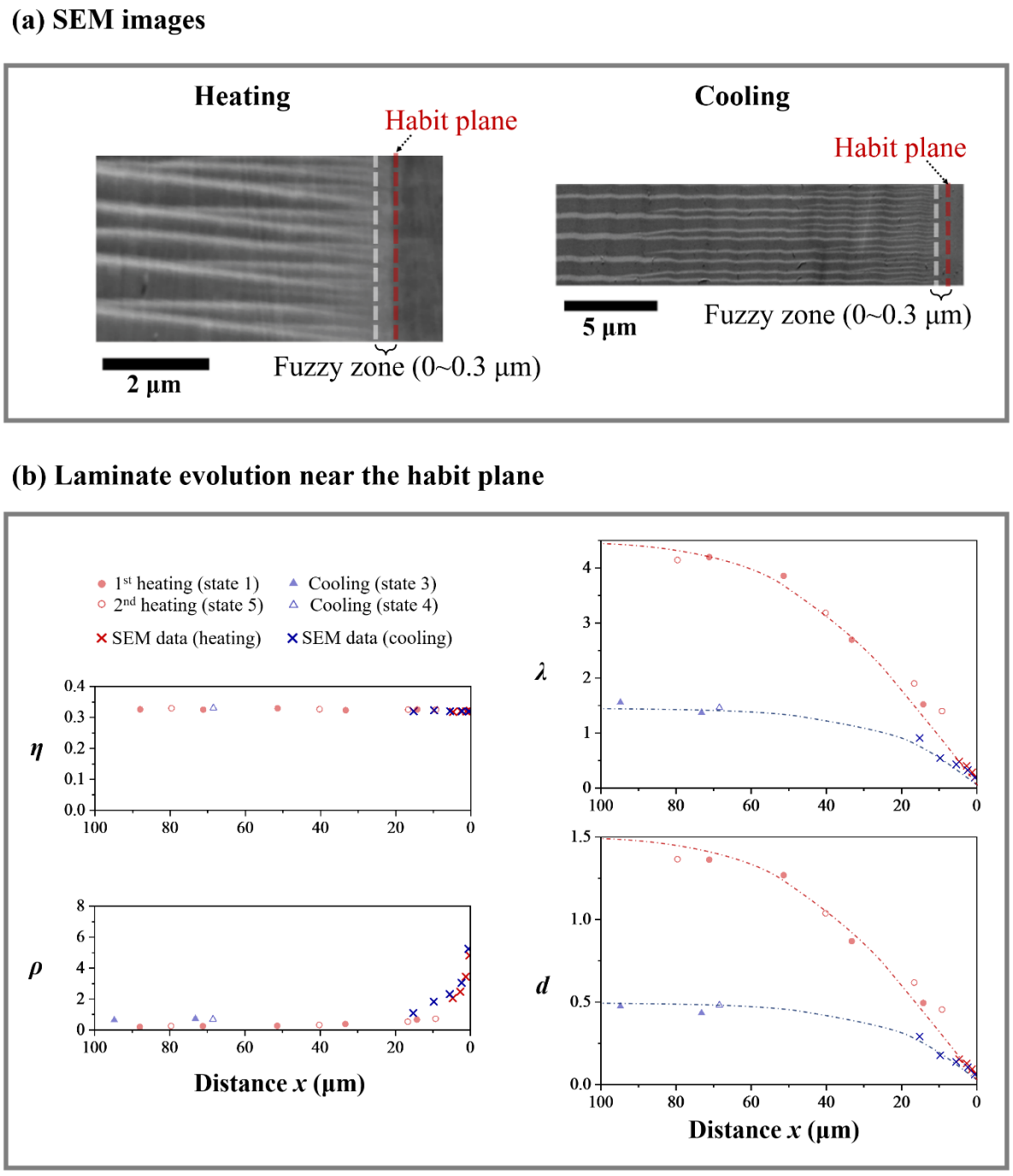

Fig. 8 (a) SEM images of the heating and cooling patterns at the zone very close to the habit plane; (b) the patterns' features η, λ, *d*, and ρ (the dash-dotted lines just guide the eyes).

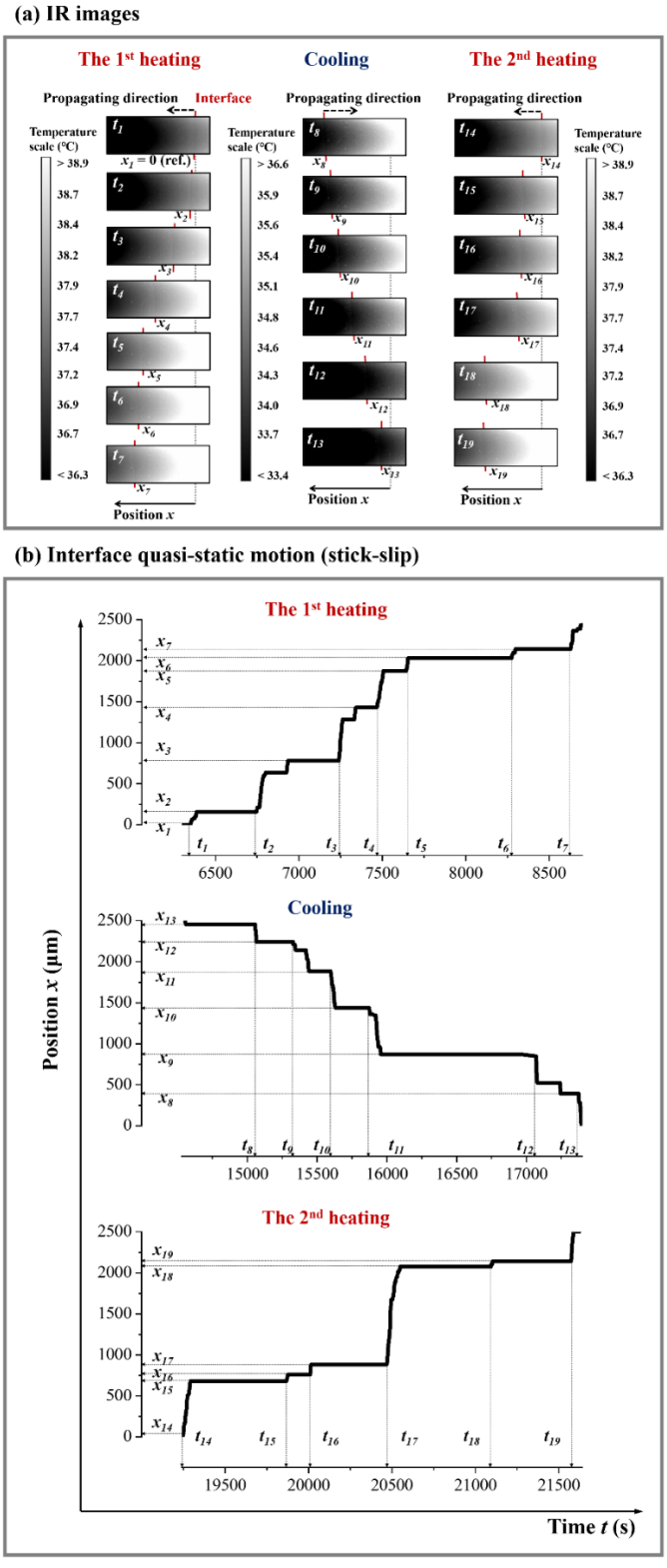

Fig. 9 (a) IR temperature measurement; (b) quasi-static interface motion during the slow heating/cooling process.

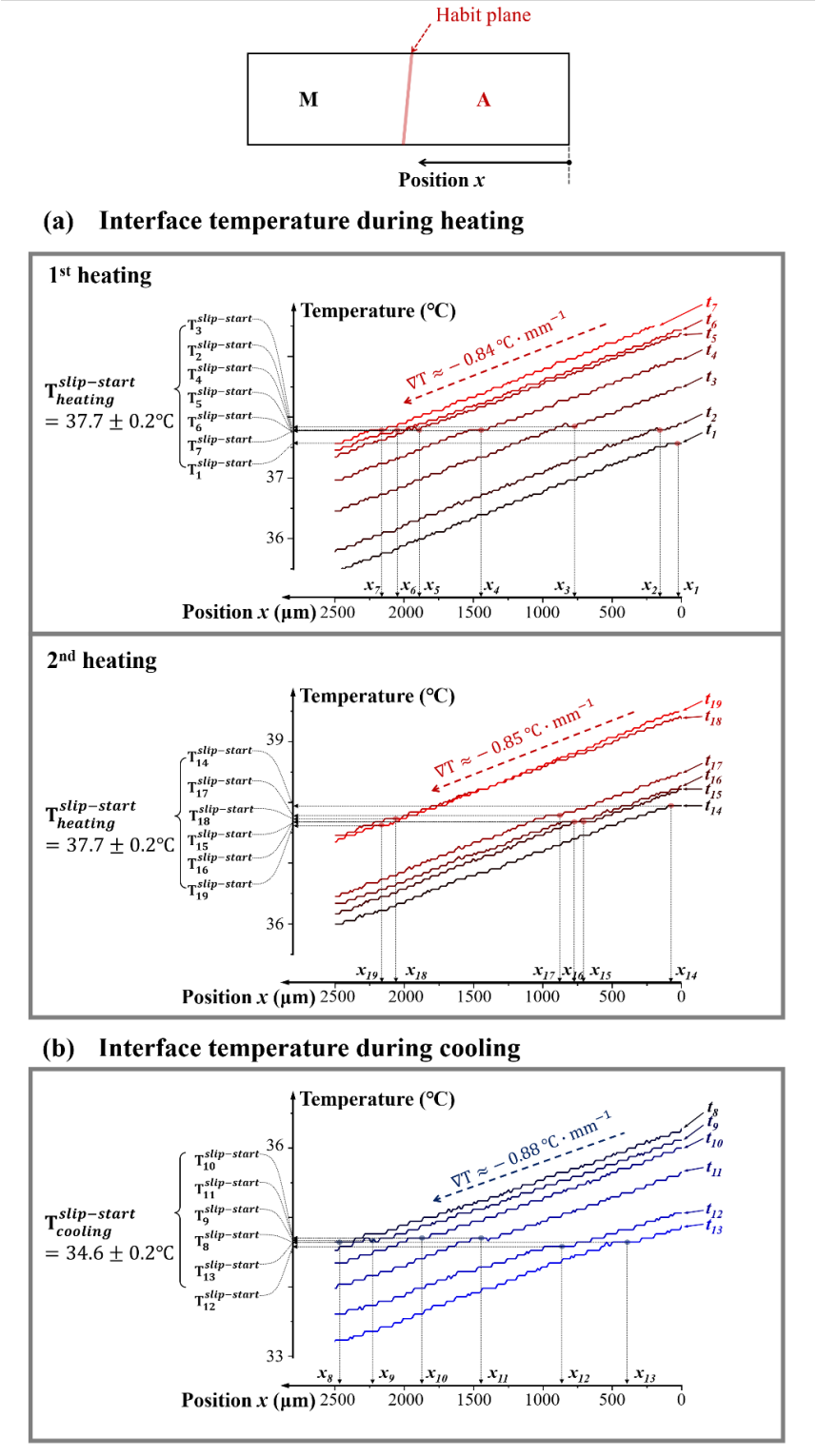

Fig. 10 Temperature profiles during heating and cooling processes.

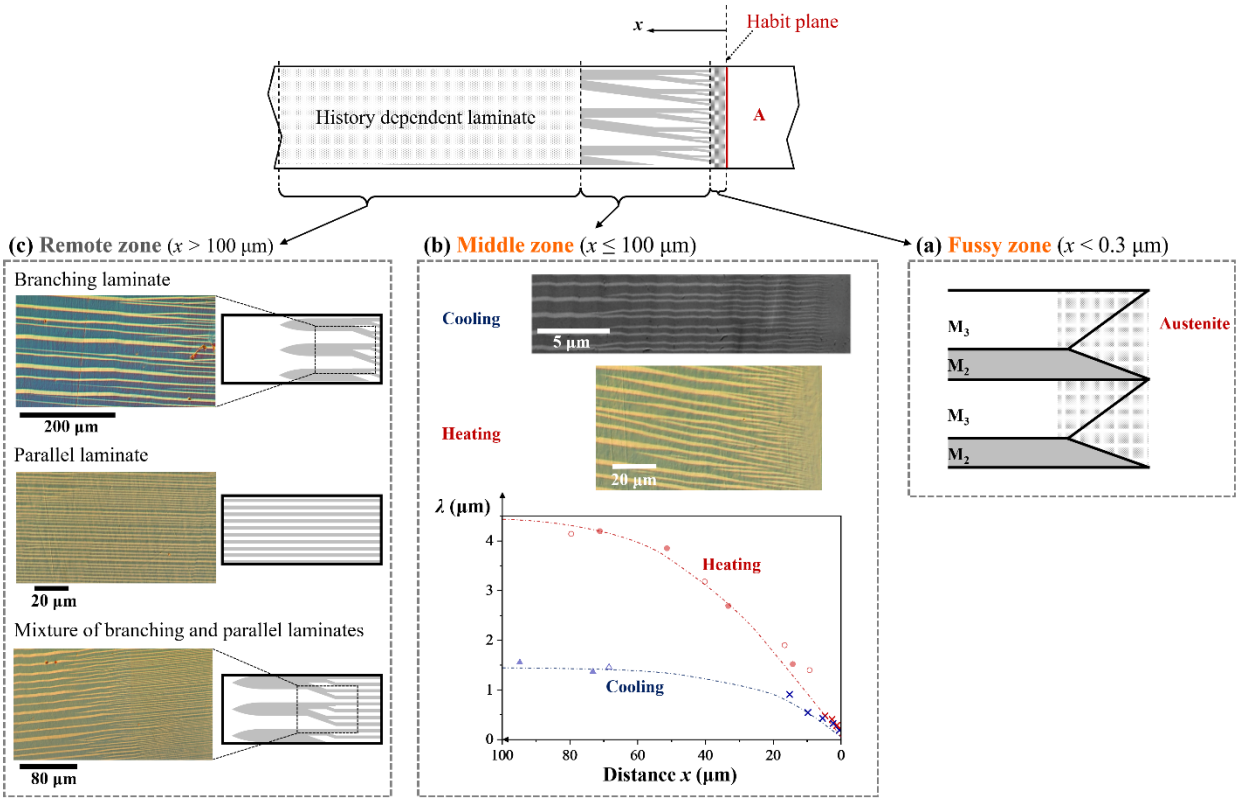

Fig. 11 The interfacial structure can be divided into three zones that have significantly different features.

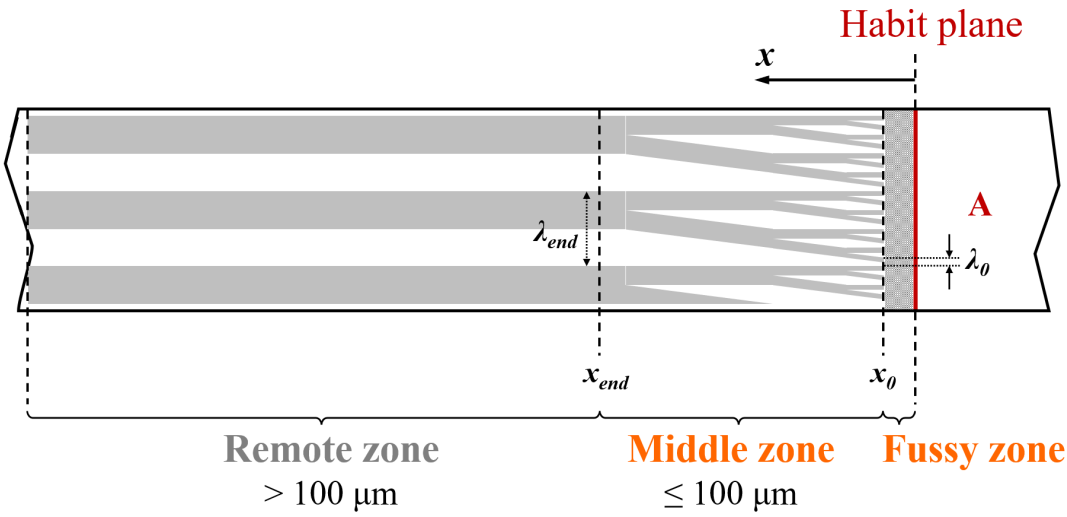

Fig. 12 Schematic of the cooling-induced interfacial structure.

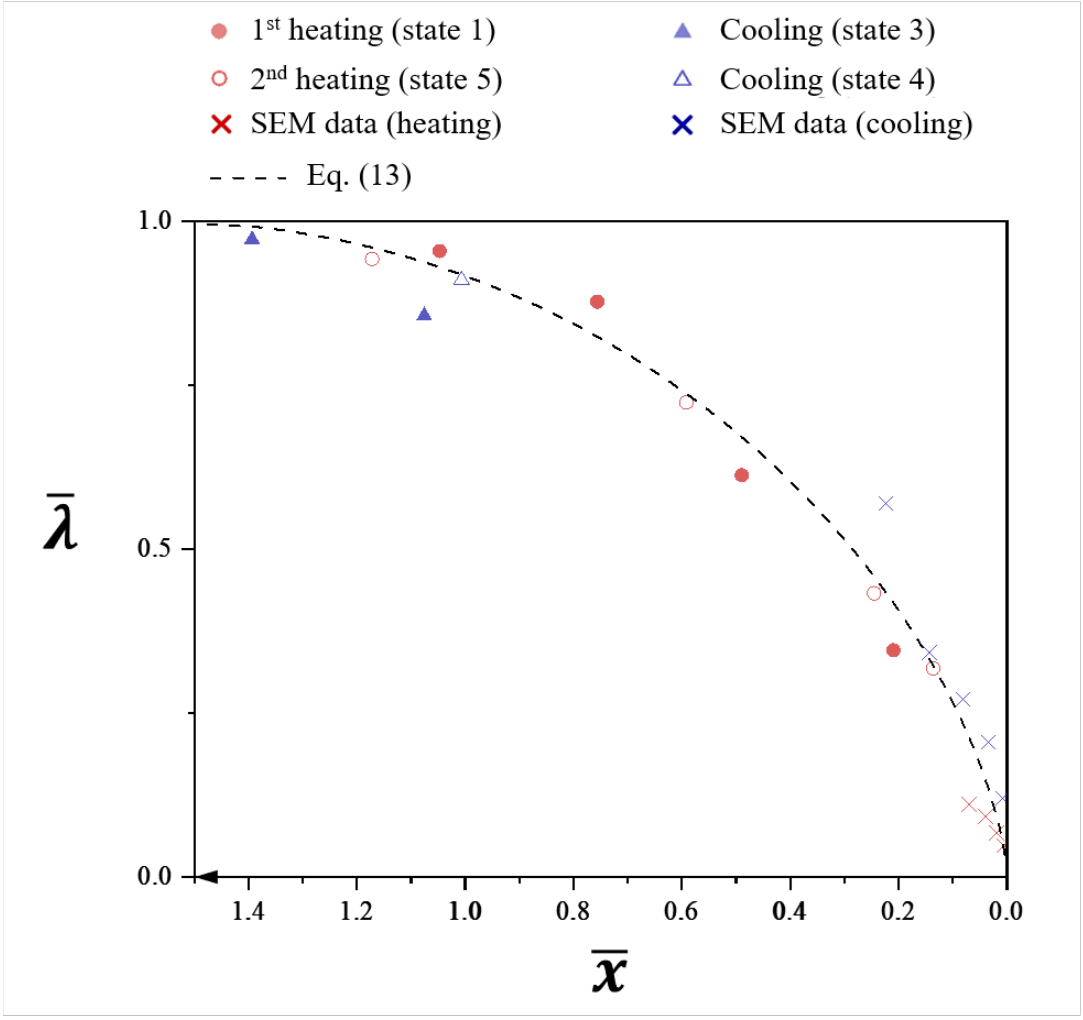

Fig. 13. Comparison between normalized experimental λ profile of the middle zone) and theoretical analysis Eq. (13). Here, $\bar{\lambda} = \frac{\lambda}{\lambda_{end}}$ and $\bar{x} = \frac{x}{l}$ are respectively the normalized laminae spacing and distance from the habit plane.

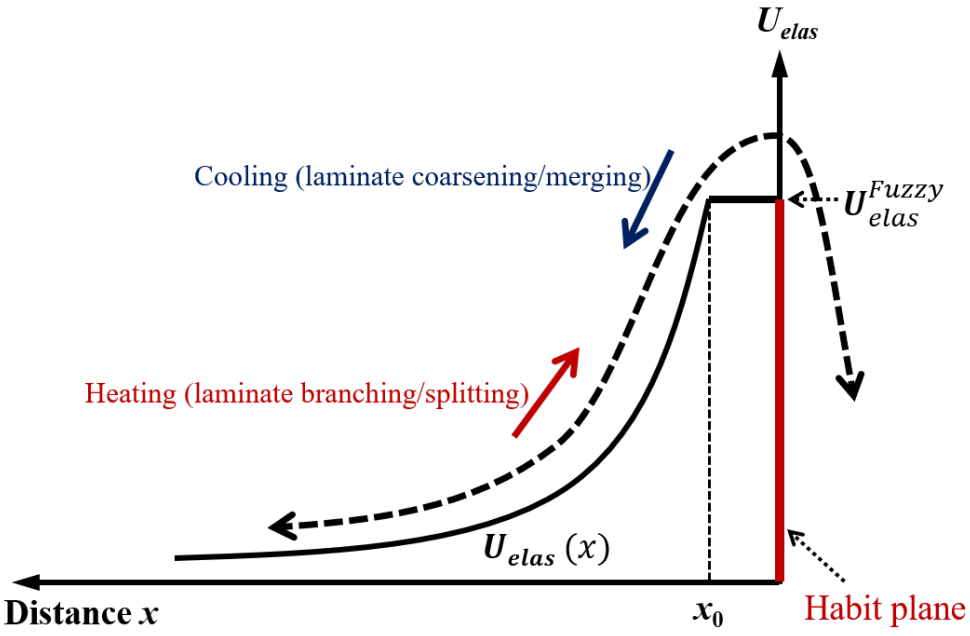

Fig. 14 Schematic of the elastic energy distribution in the interfacial structure (middle zone and the fuzzy zone).

Reference

[1] K. Ullakko, P.G. Takovenko, V.G. Gavriljuk, New developments in actuator materials as reflected in magnetically controlled shape memory alloys and high-strenghth shape memory steels, Smart structures and materials 1996: Mathematics and control in smart structures, Society of Photo-Optical Instrumentation Engineers, San Diego, CA, United States, 1996, p. Proc. 2715.

[2] R. Chulist, P. Czaja, T. Tokarski, M. Faryna, Martensite stabilisation in single crystalline Ni-Mn-Ga and Ni-Mn-Sn magnetic shape memory alloys,Mater. Lett. 230 (2018) 266-269.

[3] R. Chulist, L. Straka, N. Lanska, A. Soroka, A. Sozinov, W. Skrotzki, Characterization of mobile type I and type II twin boundaries in 10M modulated Ni–Mn–Ga martensite by electron backscatter diffraction,Acta Mater. 61(6) (2013) 1913-1920.

[4] O. Heczko, L. Straka, H. Seiner, Different microstructures of mobile twin boundaries in 10M modulated Ni–Mn–Ga martensite,Acta Mater. 61(2) (2013) 622-631.

[5] S. Zhang, X. Chen, Z. Moumni, Y.J. He, Thermal effects on high-frequency magnetic-field-induced martensite reorientation in ferromagnetic shape memory alloys: An experimental and theoretical investigation,Int. J. Plasticity 108 (2018) 1-20.

[6] S. Zhang, X. Chen, Z. Moumni, Y.J. He, Coexistence and compatibility of martensite reorientation and phase transformation in high-frequency magnetic-field-induced deformation of Ni-Mn-Ga single crystal,Int. J. Plasticity 110 (2018) 110-122.

[7] X. Chen, Y.J. He, Thermo-magneto-mechanical coupling dynamics of magnetic shape memory alloys,Int. J. Plasticity 129 (2020) 102686.

[8] X. Chen, Z. Moumni, Y.J. He, W. Zhang, A three-dimensional model of magneto-mechanical behaviors of martensite reorientation in ferromagnetic shape memory alloys,J. Mech. Phys. Solids 64 (2014) 249-286.

[9] M. Kohl, M. Gueltig, V. Pinneker, R. Yin, F. Wendler, B. Krevet, Magnetic Shape Memory Microactuators,Micromachines-Basel 5(4) (2014) 1135-1160.

[10] M. Zelený, P. Sedlák, O. Heczko, H. Seiner, P. Veřtát, M. Obata, T. Kotani, T. Oda, L. Straka, Effect of electron localization in theoretical design of Ni-Mn-Ga based magnetic shape memory alloys,Materials & Design (2021).

[11] C. Zhang, G. Qin, S. Zhang, X. Chen, Y.J. He, Hysteresis effect on austenite-martensite interface in Ni-Mn-Ga single crystal,Scripta Mater. 222 (2023) 115029.

[12] G. Qin, C. Zhang, S. Zhang, X. Chen, Y.J. He, Compatibility effect on stress-free two-way memory of Ni-Mn-Ga single crystal,J. Alloy Compd. 935 (2023) 168134.

[13] H. Seiner, P. Plucinsky, V. Dabade, B. Benešová, R.D. James, Branching of twins in shape memory alloys revisited,J. Mech. Phys. Solids 141 (2020) 103961.

[14] E. Bronstein, E. Faran, D. Shilo, Analysis of austenite-martensite phase boundary and twinned microstructure in shape memory alloys: The role of twinning disconnections,Acta Mater. 164 (2019) 520-529.

[15] S. Stupkiewicz, A. Górzyńska-Lengiewicz, Almost compatible X-microstructures in CuAlNi shape memory alloy,Continuum Mechanics and Thermodynamics 24(2) (2012) 149-164.

[16] C. Zhang, X. Balandraud, Y.J. He, Coexistence of five domains at single propagating interface in single-crystal Ni-Mn-Ga Shape Memory Alloy,J. Mech. Phys. Solids 183 (2024) 105481.

[17] K. Bhattacharya, Microstructure of Martensite: Why it Forms and How it Gives Rise to the Shape-memory Effect, Oxford University Press, Oxford, 2003.

[18] C. Zhang, X. Chen, O. Hubert, Y. He, Characterization on thermal hysteresis of shape memory alloys via macroscopic interface propagation,Materialia 33 (2024) 102038.

[19] Y.J. He, Interface propagation and energy dissipation in Shape Memory Alloys,Scripta Mater. 230 (2023) 115420.

[20] Z. Zhang, R.D. James, S. Müller, Energy barriers and hysteresis in martensitic phase transformations,Acta Mater. 57(15) (2009) 4332-4352.

[21] S. Stupkiewicz, M. Rezaee-Hajidehi, H. Petryk, Multiscale analysis of the effect of interfacial energy on non-monotonic stress–strain response in shape memory alloys,Int. J. Solids struct. 221 (2021) 77-91.

[22] K. Tůma, S. Stupkiewicz, H. Petryk, Size effects in martensitic microstructures: Finite-strain phase field model versus sharp-interface approach,J. Mech. Phys. Solids 95 (2016) 284-307.

[23] S. Stupkiewicz, G. Maciejewski, H. Petryk, Elastic micro-strain energy of austenite–martensite interface in NiTi,Modelling and Simulation in Materials Science and Engineering 20(3) (2012).

[24] S. Stupkiewicz, G. Maciejewski, H. Petryk, Low-energy morphology of the interface layer between austenite and twinned martensite,Acta Mater. 55(18) (2007) 6292-6306.

[25] O. Heczko, N. Lanska, O. Soderberg, K. Ullakko, Temperature variation of structure and magnetic properties of Ni–Mn–Ga magnetic shape memory alloys,J. Magn. Magn. Mater. 242-245 (2002) 1446-1449.

[26] S.J. Murray, M. Marioni, S.M. Allen, R.C. O'Handley, T.A. Lograsso, 6% magnetic-field-induced strain by twin-boundary motion in ferromagnetic Ni–Mn–Ga,Appl. Phys. Lett. 77(6) (2000) 886-888.

[27] M. Kök, Y. Aydoğdu, Effect of composition on the thermal behavior of NiMnGa alloys,Journal of Thermal Analysis and Calorimetry 113(2) (2012) 859-863.

[28] J.-h. Kim, F. Inaba, T. Fukuda, T. Kakeshita, Effect of magnetic field on martensitic transformation temperature in Ni–Mn–Ga ferromagnetic shape memory alloys,Acta Mater. 54(2) (2006) 493-499.

[29] S.Y. Yu, Z.X. Cao, L. Ma, G.D. Liu, J.L. Chen, G.H. Wu, B. Zhang, X.X. Zhang, Realization of magnetic field-induced reversible martensitic transformation in NiCoMnGa alloys,Appl. Phys. Lett. 91(10) (2007).

[30] J.F. Duan, P. Huang, H. Zhang, Y. Long, G.H. Wu, R.C. Ye, Y.Q. Chang, F.R. Wan, Magnetic entropy changes of NiMnGa alloys both on the heating and cooling processes,J. Alloy Compd. 441(1-2) (2007) 29-32.

[31] S.Y. Yu, S.S. Yan, S.S. Kang, X.D. Tang, J.F. Qian, J.L. Chen, G.H. Wu, Magnetic field-induced martensite–austenite transformation in Fe-substituted NiMnGa ribbons,Scripta Mater. 65(1) (2011) 9-12.

[32] S. Singh, J. Bednarcik, S.R. Barman, C. Felser, D. Pandey, Premartensite to martensite transition and its implications for the origin of modulation inNi2MnGaferromagnetic shape-memory alloy,Phys. Rev. B 92(5) (2015).

[33] L. Mañosa, A. Gonzàles-Comas, E. Obrado, A. Planes, V.A. Chernenko, V.V. Kokorin, E. Cesari, Anomalies related to the TA_2-phonon-mode condensation in Heusler Ni2MnGa alloy,Phys. Rev. B 55(17) (1997) 11068-11071.

[34] G. Fritsch, V.V. Kokorin, A. Kempf, Soft modes in Ni_2MnGa single crystals,Journal of physics: condensed matter 6 (1994) L107-L110.

[35] L. Dai, J. Cullen, M. Wuttig, Intermartensitic transformation in a NiMnGa alloy,J. Appl. Phys. 95(11) (2004) 6957-6959.

[36] Q. Hu, H. Luo, C. Li, L. Vitos, R. Yang, Composition dependent elastic modulus and phase stability of Ni2MnGa based ferromagnetic shape memory alloys,Science China Technological Sciences 55(2) (2011) 295-305.

[37] J. Worgull, E. Petti, J. Trivisonno, Behaviour of the elastic properties near an intermediate phase transition in Ni_2MnGa,Phys. Rev. B 54(22) (1996) 15695.

[38] J.M. Ball, R.D. James, Fine phase mixtures as minimizers of energy, Springer, Berlin, Heidelberg, 1989.

[39] R.V. Kohn, S. Müller, Branching of twins near an austenite—twinned-martensite interface,Philos. Mag. A 66(5) (1992) 697-715.

[40] A. Diestel, A. Backen, U.K. Rößler, L. Schultz, S. Fähler, Twin boundary energy of hierarchically twinned magnetic shape memory alloys,Appl. Phys. Lett. 99(9) (2011).